Solder Ball
Connect (SBC)
assemblies
under thermal
loading:
II. Strain analysis
via image
processing,
and reliability
considerations

by H.-C. Choi Y. Guo W. LaFontaine C. K. Lim

A novel approach to processing interferometric moiré images, called computational Fourier transform moiré, has been developed. The essential principle of this technique is to automatically calculate a whole-field strain from digitized images of interferometric moiré fringes using digital Fourier transform procedures. With the use of this technique, a whole-field strain distribution of a Solder Ball Connect (SBC) interconnection under thermal loading was obtained. The calculated strain field was then used to understand fatigue modes of SBC observed from an accelerated thermal cycling (ATC) test.

Introduction

The reliability of Solder Ball Connect (SBC), a technology for connecting—both physically and electrically—multilayer ceramic modules containing one or more chips to printed circuit boards by means of small balls of solder [1, 2], depends on the fatigue behavior of the solder joints. The fatigue of SBC interconnections is primarily caused by thermal loading. In turn, the strain induced by the thermal loading depends mainly upon the mismatches of coefficients of thermal expansion between the ceramic modules and the boards. To characterize an SBC failure, therefore, a detailed deformation analysis is required. Moiré interferometry, a high-resolution experimental method for measuring whole-field

****Copyright** 1993 by International Business Machines Corporation. Copying in printed form for private use is permitted without payment of royalty provided that (1) each reproduction is done without alteration and (2) the *Journal* reference and IBM copyright notice are included on the first page. The title and abstract, but no other portions, of this paper may be copied or distributed royalty free without further permission by computer-based and other information-service systems. Permission to *republish* any other portion of this paper must be obtained from the Editor.

deformations (deformations of regions rather than points), is one technique used for this purpose. With this method, Guo et al. [1], in Part I of this paper, were able to obtain the deformation field of an entire SBC assembly as well as the deformation fields of the individual solder ball interconnections.

Because moiré fringes contain phase information concerning displacement fields, additional data processing is required to obtain whole-field strains. A new tool for such data processing, a technique called the computational Fourier transform moiré (CFTM) method, is presented in this paper. This image processing tool can automatically extract the whole-field strains from digitized interferometric moiré images.

After briefly describing the mathematical essence of the CFTM method, this paper presents the whole-field strain distribution of an SBC interconnection. Finally, an attempt is made to correlate the calculated strain field with the observed fatigue modes of SBC interconnections in accelerated thermal cycling (ATC) tests.

Computational Fourier transform moiré (CFTM) method

This section briefly describes the essential principle of the CFTM method, by which a whole-field strain can be automatically extracted from digitized interferometric moiré images.

• Conventional strain analysis method

Consider the in-plane¹ deformation field $\mathbf{u} = (u_1, u_2)$ in the $\mathbf{x} = (x_1, x_2)$ space. (In Part I of this paper, U and V are used to denote the deformation fields rather than u_1 and u_2 used here. Part I denotes directions as x and y rather than x_1 and x_2 .) With the use of a linear reference grating, moiré interferometry measures a displacement component perpendicular to the reference grating lines. As shown by Shield and Kim² [3], the fringe order N_{α} at a point \mathbf{x} can be written as

$$N_{\alpha} = \mathbf{G}_{\alpha} \cdot \mathbf{u} + (\mathbf{g}_{\alpha} - \mathbf{G}_{\alpha}) \cdot \mathbf{x}, \tag{1}$$

where \mathbf{g}_{α} and \mathbf{G}_{α} are the reciprocal grating vectors of the reference and specimen gratings, respectively, in the undeformed configuration. A reciprocal grating vector has a direction that is perpendicular to the grating lines and a magnitude equal to the reciprocal of the grating spacing. In order to use Equation (1) to determine the in-plane deformation completely, two sets of reference and specimen gratings (\mathbf{g}_1 , \mathbf{G}_1) and (\mathbf{g}_2 , \mathbf{G}_2) must be used. Greek subscripts α and β (= 1 or 2) are used to denote which of two sets of reference and specimen gratings and which of the quantities being measured with those sets of

gratings are considered. The last term in Equation (1), $(\mathbf{g}_{\alpha} - \mathbf{G}_{\alpha}) \cdot \mathbf{x}$, represents the carrier pattern in the moiré fringes [3]. Even though carrier patterns are not related to the actual deformation of a body, they add constant strain values to the actual strain fields. To extract actual strain fields, therefore, constant strain values produced by carrier patterns must be eliminated. In many applications, a square grating is used as a specimen grating. When such a moiré interferometry system is set up, two reference gratings are aligned with the square grating of the specimen, and their spacings are adjusted to be equal to the corresponding spacings of the specimen grating. In this case, the moiré fringes contain no carrier patterns, and Equation (1) is reduced to Equation (1) of Part I [1]. Note that Equation (1) holds for orthogonal as well as nonorthogonal pairs of reference and specimen gratings.

To calculate the displacement and strain at a point, Equations (1) and (2) of Part I can be used directly. Digital processing is required to calculate the displacement and strain distributions within regions. The simplest method of accomplishing this is by use of Equation (1), which represents the constant-phase information of the actual moiré fringes. Here, only the fringe locations are needed to calculate the displacements and strains. Thus, the first data processing step is to reduce the fringe patterns to two-level images through binarization. Because fringe orders are assigned to fringe edges (the boundaries between the black and white fringes of the binarized moiré image), the threshold level is the key factor controlling the accuracy of data processing. When the actual moiré images are formed, both displacement information and background noise are involved. The background noise produced by nonuniform illumination and nonuniform specimen gratings changes very slowly within the region compared to the moiré fringes. To locate the fringe edges accurately, the threshold level should be locally adjusted. The simplest method of doing that is to binarize the moiré images according to local averages determined within a certain window size. The best method of eliminating the background noise is image subtraction using a phaseshifting method, as discussed in [3, 4] and footnote 2. In the following, the phase-shifting method is very briefly reviewed.

The actual intensity distribution of the moiré fringes without any carrier patterns, $\tilde{I}_{c}(\mathbf{x})$, can be written as

$$\widetilde{I}_{\alpha}(\mathbf{x}) = \widetilde{I}_{0\alpha} e^{-2\pi i \mathbf{G}_{\alpha} \cdot \mathbf{u}} + I_{bg}(\mathbf{x}), \tag{2}$$

where $\tilde{I}_{0\alpha}$ is the amplitude of the moiré fringe pattern and $I_{bg}(\mathbf{x})$ is a low-frequency background noise. Note that Equation (1) represents the phase term of the actual moiré fringes defined by Equation (2). The constant-phase term can be added to the moiré fringes by changing the optical path or by changing the direction of polarization of the system (for a detailed discussion and hardware setup,

¹ In this paper "in-plane" refers to the plane of the reference grating.
2 T. W. Shield and K.-S. Kim, "An Experimental Study of the Plastic Deformation Fields Near a Crack Tip in an Iron-Silicon Single Crystal," unpublished work, 1993.

see [3, 4]). The intensity distribution of the shifted moiré fringes, $\tilde{I}'_{\alpha}(\mathbf{x})$, is written as

$$\widetilde{I}'_{\alpha}(\mathbf{x}) = \widetilde{I}_{0\alpha} e^{-2\pi i (\mathbf{G}_{\alpha} \mathbf{u} + \phi)} + I_{bg}(\mathbf{x}), \tag{3}$$

where ϕ is the amount of the phase shift. Note that the background noise remains unchanged. Subtraction of Equation (3) from (2) gives

$$I_{\alpha}(\mathbf{x}) = I_{0\alpha} e^{-2\pi i \mathbf{G}_{\alpha} \cdot \mathbf{u}},\tag{4}$$

where $I_{0\alpha}=2\tilde{I}_{0\alpha}$. For the best contrast of moiré fringes, the amount of phase shift is 180° [3, 4]; this value was chosen for the experiment described here. In Equation (4), the background noise in the moiré fringes has been eliminated. This process also subtracts any false images produced by the imaging system itself.

Once a proper binary image is obtained, the fringe edges can easily be traced, and the corresponding fringe orders assigned to the traced line segments. These traced fringe data can be used to interpolate the fractional fringe order on evenly spaced points within the region. Then the displacements and strains can easily be calculated at these evenly spaced points. The detailed algorithm can be found in [3] and footnote 2. The accuracy of the calculated displacements and strains depends on the accuracy of fringe edge tracing, which in turn depends upon aspects of the preprocessing of the moiré images, such as the threshold level of binarization and the smoothing method. The error in calculating displacements and strains is the sum of the individual errors of each processing step. Because of the necessary human input, systematic error control is not easily accomplished in this case. Also, it is not easy to automate the data processing, because the assignment of fringe orders to the individual fringes requires human interaction.

• Direct computational Fourier transform moiré (DCFTM) method

To eliminate these difficulties, Fourier transforms can be used to obtain the displacements and strains of a deformed body without the aid of a moiré interferometry system. With this technique, known as the direct computational Fourier transform moiré (DCFTM) method, moiré fringes are computationally generated from the digitized image of a deformed specimen grating that was originally uniformly spaced and whose original spacing is known.

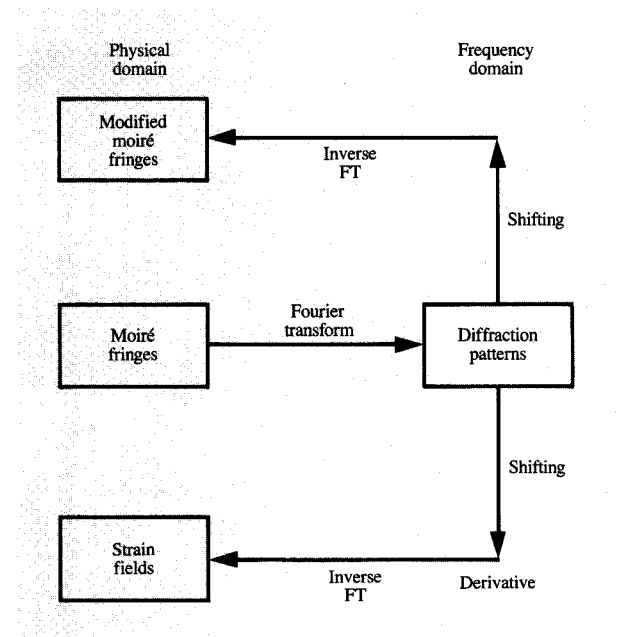
A moiré interferometry system chooses two diffraction orders and aligns them along an optical axis to form an interference fringe at the image plane. Mathematically, the choice of diffraction orders is equivalent to the choice of diffraction patterns of a deformed grating in the Fourier transform plane (frequency domain). Also, the alignment along the optical axis means the shifting of the diffraction pattern by the amount of a corresponding diffraction order.

The displacement sensitivity depends upon the diffraction order involved in the system. The imaging of moiré fringes is simply an inverse Fourier transform operation on the shifted diffraction pattern. Using this principle, Morimoto et al. [5] were able to obtain a strain field by applying Fourier transforms directly to a deformed linear grating of a specimen, and Choi et al. [6] were successful in extracting the deformation field near a dislocation from a high-resolution electron microscopy atomic image. Choi et al. calculated the strains directly by the inverse Fourier transforms of the derivatives of diffraction patterns, while Morimoto et al. used Equation (1) to obtain strains, a process which requires the unwrapping of phase information of actual moiré fringes from Equation (4). Note that the method used in [6] requires more computation because of additional Fourier transforms but does not require the undesirable unwrapping process.

The DCFTM method discussed above has advantages. For example, the data processing scheme can be almost fully automated and error can be systematically controlled, because the only operations involved in the method are Fourier transforms and the establishment of diffraction windows to choose the diffraction patterns. On the other hand, the spatial resolution is limited by the number of pixels of the imaging system, while the spatial resolution of optical systems is of the order of the wavelength of light. With the DCFTM method, the field of a region of interest is limited to several tens of grating lines; however, this method may be useful for analyzing the deformation field within a very small region (less than $100~\mu m \times 100~\mu m$). In this case, a high-resolution SEM can be used to scan fine deformed gratings.

To apply the Fourier transform method discussed above to a large region of interest, which may contain thousands of grating lines, Fourier transforms can be applied to moiré fringe images produced by a moiré interferometry system rather than directly to the deformed specimen grating. In this case, the moiré interferometry system plays the role of an optical data-reduction filter. Combining the two methods permits complete automation of the data processing necessary to obtain displacements and strains and covers a large area. This new technique, called the computational Fourier transform moiré (CFTM) method, is discussed in the following section.

• Computational Fourier transform moiré (CFTM) method. To apply the CFTM method, the number of interferometric moiré fringes should be sufficient to produce a well-defined diffraction pattern. This can easily be done by introducing a certain amount of carrier pattern, either by rotating a reference grating or by changing the spacing of the reference grating [see Equation (1)]. The carrier pattern produced in either way represents a constant strain value throughout the region and is eliminated during subsequent



Schematic of the computational Fourier transform moiré (CFTM) method.

data processing. In this paper, only the rotational carrier pattern is used. With the carrier pattern given in Equation (1), Equation (4) can be written as

$$I_{\alpha}(\mathbf{x}) = I_{0\alpha} e^{-2\pi i (\mathbf{G}_{\alpha} \cdot \mathbf{u} - \mathbf{k}_{\alpha} \cdot \mathbf{x})}, \tag{5}$$

where carrier pattern \mathbf{k}_{α} is given by $\mathbf{G}_{\alpha} - \mathbf{g}_{\alpha}$. Note that the average spacing of moiré fringes modulated by a carrier pattern depends on the magnitude of \mathbf{k}_{α} .

To obtain strains, Fourier transforms are applied to the modulated moiré fringes in Equation (5). The Fourier transform of $I_{\mathbf{x}}(\mathbf{x})$ is given by

$$I_{\alpha}^{*}(\mathbf{k}) = \frac{1}{2\pi} \int_{\mathcal{A}_{\alpha}} I_{0\alpha} e^{-2\pi i \mathbf{G}_{\alpha} \mathbf{u}} e^{-2\pi i (\mathbf{k} - \mathbf{k}_{\alpha}) \mathbf{x}} d\mathbf{x}, \tag{6}$$

where k is the frequency domain variable within the frequency domain A_k , and A_x represents the region of interest in the moiré image. The interferometric moiré fringes without a carrier pattern can be constructed as follows. First, the diffraction pattern given by Equation (6) is shifted in order to eliminate the carrier pattern by substituting

$$\tilde{\mathbf{k}} = \mathbf{k} - \mathbf{k}_{\alpha}.\tag{7}$$

Then an inverse Fourier transform of the shifted diffraction pattern reconstructs the moiré fringes, and the constant strain value added by the carrier pattern is eliminated. The moiré fringe pattern generated by an inverse Fourier transform is given by

$$I_{0\alpha}e^{-2\pi i\mathbf{G}_{\alpha}\cdot\mathbf{u}} = \frac{1}{2\pi} \int_{A_{\mathbf{k}}} I_{\alpha}^{*}(\widetilde{\mathbf{k}})e^{2\pi i\widetilde{\mathbf{k}}\cdot\mathbf{x}} d\widetilde{\mathbf{k}}, \tag{8}$$

where A_{k} is the integration domain which is the same as A_{k} but shifted by Equation (7). The moiré fringe pattern of Equation (8) is exactly the same as that of Equation (4). A strain field may then be calculated directly from the above moiré fringe pattern by unwrapping phase information, as in [5]. Even though this technique saves computational time, the unwrapping process requires careful treatment to result in a continuous displacement field, and a smoothing process is needed before taking derivatives of displacements to obtain the strain. To avoid these undesirable processes, Choi et al. [6] developed a direct method of calculating the strain. In that method, a strain field is constructed directly from the diffraction patterns of Equation (6) rather than from the phase information of the moiré fringes of Equation (1). When the gradient of Equation (8) with respect to the deformed coordinates is taken directly, the directional displacement gradient vector is given by

$$\mathbf{G}_{\alpha} \cdot \nabla \mathbf{u} = -\frac{\int_{A_{\mathbf{k}}} \widetilde{\mathbf{k}} I_{\alpha}^{*}(\widetilde{\mathbf{k}}) e^{2\pi i \widetilde{\mathbf{k}} \mathbf{x}} d\widetilde{\mathbf{k}}}{\int_{A_{\mathbf{k}}} I_{\alpha}^{*}(\widetilde{\mathbf{k}}) e^{2\pi i \widetilde{\mathbf{k}} \mathbf{x}} d\widetilde{\mathbf{k}}}.$$
(9)

From this equation, four components of the displacement gradient tensor can easily be calculated from the diffraction patterns by

$$\tilde{u}_{\alpha,\beta} = -\frac{\int_{A_{\tilde{\mathbf{k}}}} (\tilde{\mathbf{k}} \cdot \mathbf{G}_{\beta}) I_{\alpha}^{*}(\tilde{\mathbf{k}}) e^{2\pi i \tilde{\mathbf{k}} \cdot \mathbf{x}} d\tilde{\mathbf{k}}}{|\mathbf{G}_{\alpha}| |\mathbf{G}_{\beta}| \int_{A_{\tilde{\mathbf{k}}}} I_{\alpha}^{*}(\tilde{\mathbf{k}}) e^{2\pi i \tilde{\mathbf{k}} \cdot \mathbf{x}} d\tilde{\mathbf{k}}},$$
(10)

where $\tilde{u}_{\alpha,\beta}$ represents a \mathbf{G}_{β} -direction derivative of a \mathbf{G}_{α} -direction displacement field, and both α and β are either 1 or 2. The above equation is valid for any nonorthogonal specimen gratings.

To calculate strain components, the x_1 and x_2 components of the displacement gradient tensor given in Equation (10) must be calculated. First, assume that specimen grating vectors \mathbf{G}_x are given by

$$\mathbf{G}_{1} = |\mathbf{G}_{1}|(a_{11}\mathbf{e}_{1} + a_{12}\mathbf{e}_{2}) \tag{11}$$

and

$$\mathbf{G}_{2} = |\mathbf{G}_{2}|(a_{21}\mathbf{e}_{1} + a_{22}\mathbf{e}_{2}), \tag{12}$$

where e_1 and e_2 are unit vectors along the x_1 and x_2 axes,

respectively. Then the displacement gradient tensor in the (x_1, x_2) coordinates is given by

$$u_{i,i} = a_{ki} a_{li} \tilde{u}_{k,l}, \tag{13}$$

where italic subscripts are used to denote physical quantities in terms of (x_1, x_2) coordinates, and conventional summation is implied on repeated indices. Because we can view the deformed configuration only in experiments, the Almansi strain is a useful measure. The Almansi strain can easily be obtained by

$$E_{ij}^{A} = \frac{1}{2} (u_{i,j} + u_{j,i} + u_{k,i} u_{k,j}). \tag{14}$$

The computation of eight Fourier transforms is involved in obtaining a complete set of strains using the CFTM method. Figure 1 is a schematic of the method.

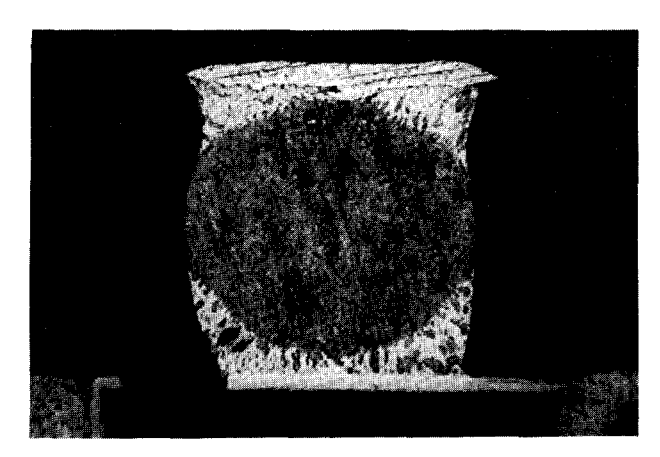
A CFTM computer program was developed to obtain whole-field strains from interferometric moiré images based on the procedure described above. It runs on a Microsoft Windows[®] environment to provide graphical handling of images, and its operations are totally menu-driven. In the next section, strain distributions of an SBC assembly are calculated by use of this CFTM program. A fast Fourier transform (FFT) algorithm is used to perform the Fourier transforms.

Strain distributions of SBC interconnections

This paper considers a 25-mm SBC assembly, which was also used in Part I of this paper [1] to study deformation. The cross section of a typical solder joint is shown in Figure 2, provided by T. Caulfield of IBM East Fishkill. The solder ball in the center (90%Pb/10%Sn) is joined both to a multilayer ceramic module (top structure in Figure 2) and to a printed circuit board (bottom structure) using eutectic solder. The material properties of these solders are strongly dependent on temperature. Detailed material properties and micro structures of an individual solder ball can be found in [2]. As pointed out in Part I, when the assembly is subjected to thermal loading, the highest strains are found in the solder balls farthest from the center of the assembly. Therefore, we consider the rightmost solder ball in the specimen shown in Figure 4 of Part I for calculating strains. Note that the specimen and the thermal loading considered here are exactly the same as in Part I of this paper.

The moiré images presented in Figure 4 of Part I were made with no added carrier patterns. The moiré fringes to which the CFTM method is applied should have an average fringe spacing from 10 to 20 pixels to avoid aliasing and interference with low-frequency noise (the zeroth-order harmonic) when Fourier transforms are applied.

Figure 3 is a set of moiré fringes of horizontal and vertical displacement fields for the rightmost solder ball



_ . . .

Typical cross section of a solder ball.

interconnection (and part of an adjacent one) in the SBC assembly considered in Part I of this paper. At the top is the multilayer ceramic module; at the bottom is the printed circuit board. The moiré fringes in Figure 3 were modulated by means of a 0.17° counterclockwise rotation of the virtual grating. Note that, because of this rigid-body rotation, moiré fringes shown in Figure 3 are different from those shown in Figure 4 of Part I. (Figure 7 of Part I also demonstrates the change of moiré fringes due to the rigidbody rotation.) A Videk[™] CCD video camera (1024 × 1024 pixels) and an ITI™ imaging system were used to digitize the moiré images. In Figure 3, only a 480 × 400-pixel region is shown with a magnification L of 4.25 μ m/pixel. These images have already been processed to eliminate background noise by means of the phase-shifting method described at the beginning of the previous section.

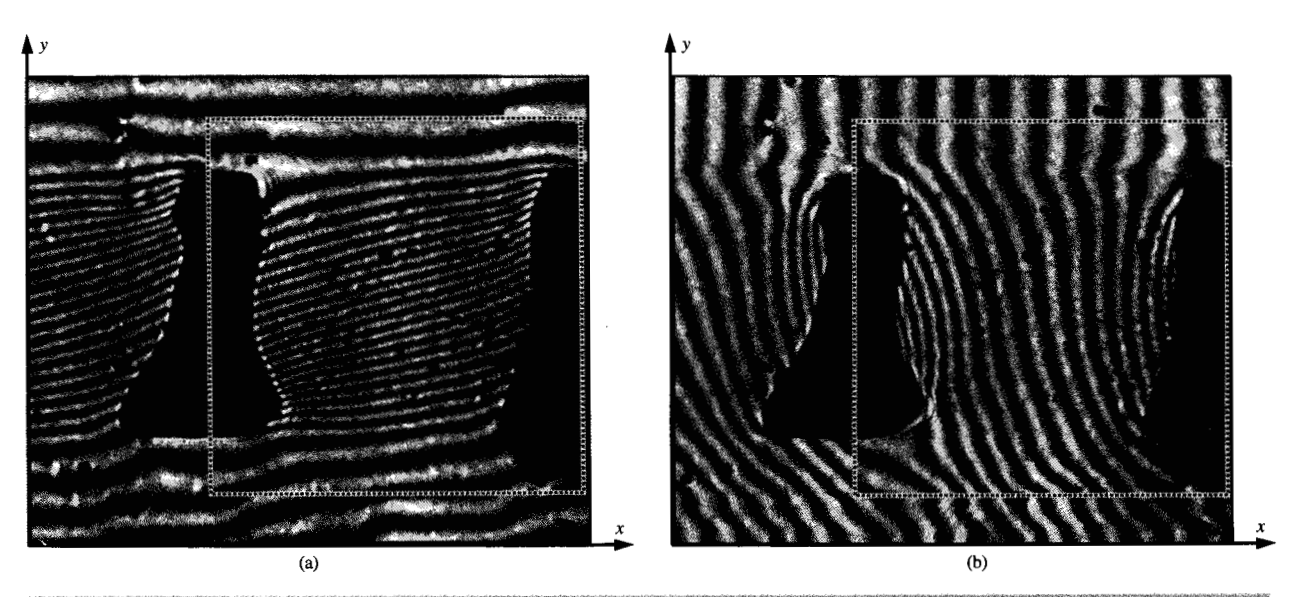
The first step in calculating strain fields is obtaining diffraction patterns. The region enclosed with a dotted line in Figure 3 (320 × 320 pixels) was considered for this purpose. The two reciprocal specimen grating vectors \mathbf{G}_{α} in Equation (5) have the same magnitude of 0.42 $(\mu m)^{-1}$ but point in the x_1 direction for the horizontal displacement field [Figure 3(a)] and in the x_2 direction for the vertical displacement field [Figure 3(b)]. Because the reciprocal reference grating vectors \mathbf{g}_{α} have the same magnitude as \mathbf{G}_{α} but are rotated by 0.17° in the counterclockwise direction from the corresponding \mathbf{G}_{α} , the carrier frequencies \mathbf{k}_{α} (= $\mathbf{G}_{\alpha} - \mathbf{g}_{\alpha}$) are given by

$$\mathbf{k}_{1} = \frac{1}{LM} (0.12\mathbf{e}_{1} - 14.9\mathbf{e}_{2}) (\mu \,\mathrm{m})^{-1}$$
 (15)

for the horizontal displacement field and

$$\mathbf{k}_{2} = \frac{1}{IM} \left(-14.9\mathbf{e}_{1} - 0.12\mathbf{e}_{2} \right) \left(\mu \mathbf{m} \right)^{-1} \tag{16}$$

653



STATE OF

Moiré fringe patterns of the cross section of an SBC specimen: (a) Horizontal displacement field; (b) vertical displacement field.

for the vertical displacement field. M is 512, the number of discrete frequencies used in calculating the diffraction pattern using the FFT method. Then diffraction patterns for both fields can be calculated with Equation (6). The magnitude of $I^*(\mathbf{k})$ is plotted in Figure 4 with 256 gray levels. (Calculating one diffraction pattern took 8 to 10 minutes on a PS/Valuepoint[™] Model 466DX2 personal computer.) Fourier transform domains were chosen to cover all frequencies of the moiré fringes in the region. The units of frequency values labeled in Figure 4 are $(pixel)^{-1}$; those values should be divided by LM(0.00218 m/pixel) to obtain the actual frequencies. For the moiré fringes shown in Figure 3, the lowest frequency is about 15/(LM) $(\mu m)^{-1}$ in the region of the module, while the highest frequency is about 58/(LM) $(\mu m)^{-1}$ near the upper right corner, between the module and the solder ball. In the figure, carrier frequencies for the horizontal and vertical field are marked with the + symbol [their values are given by Equations (15) and (16)].

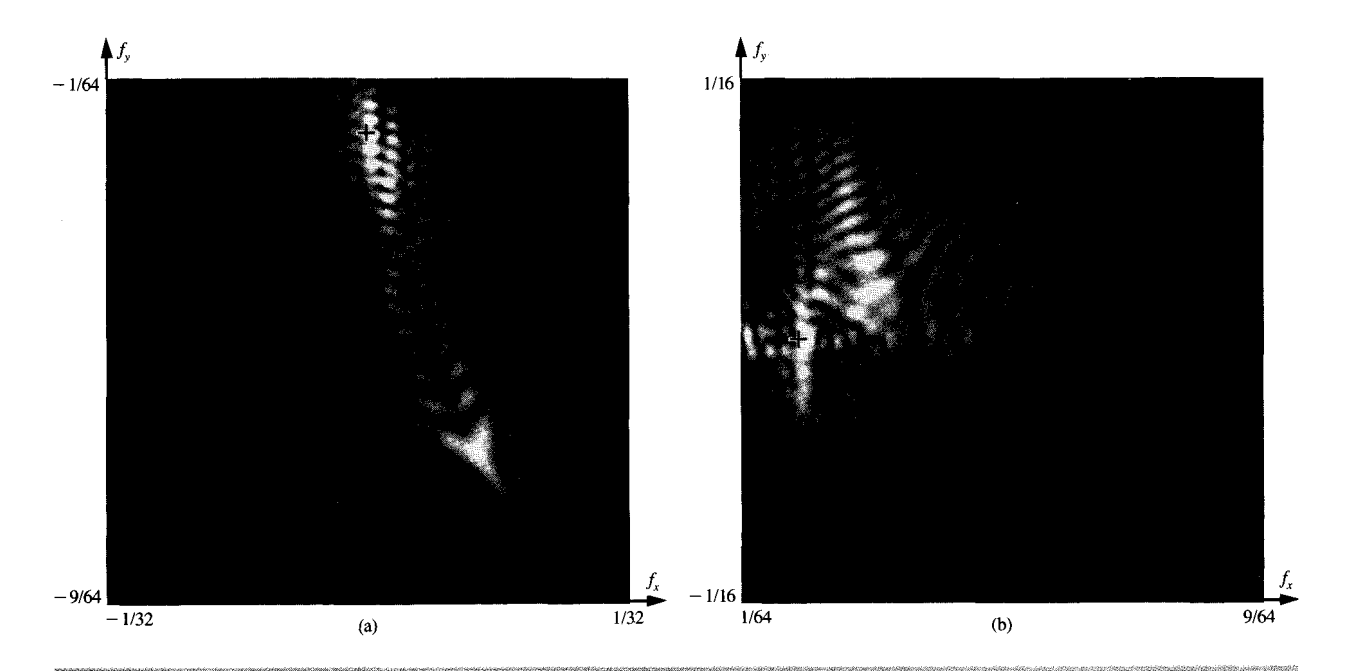
Reconstruction of modified moiré fringes can be done by an inverse Fourier transform of the diffraction pattern after the diffraction pattern is shifted according to Equation (7). This shifting procedure removes the rigid-body rotation that was intentionally introduced in Figure 3. These modified moiré fringes are shown in Figure 5. (Only the part of the figure inside the box has been processed.) Next, a displacement gradient tensor can easily be calculated with Equation (10). This requires a total of six inverse Fourier transforms applied to derivatives of the diffraction patterns. Then strain components are given by

Equation (14) in terms of components of the displacement gradient tensor. These strain components, due to the thermal loading of the -60° C temperature change, are shown in **Figure 6**.

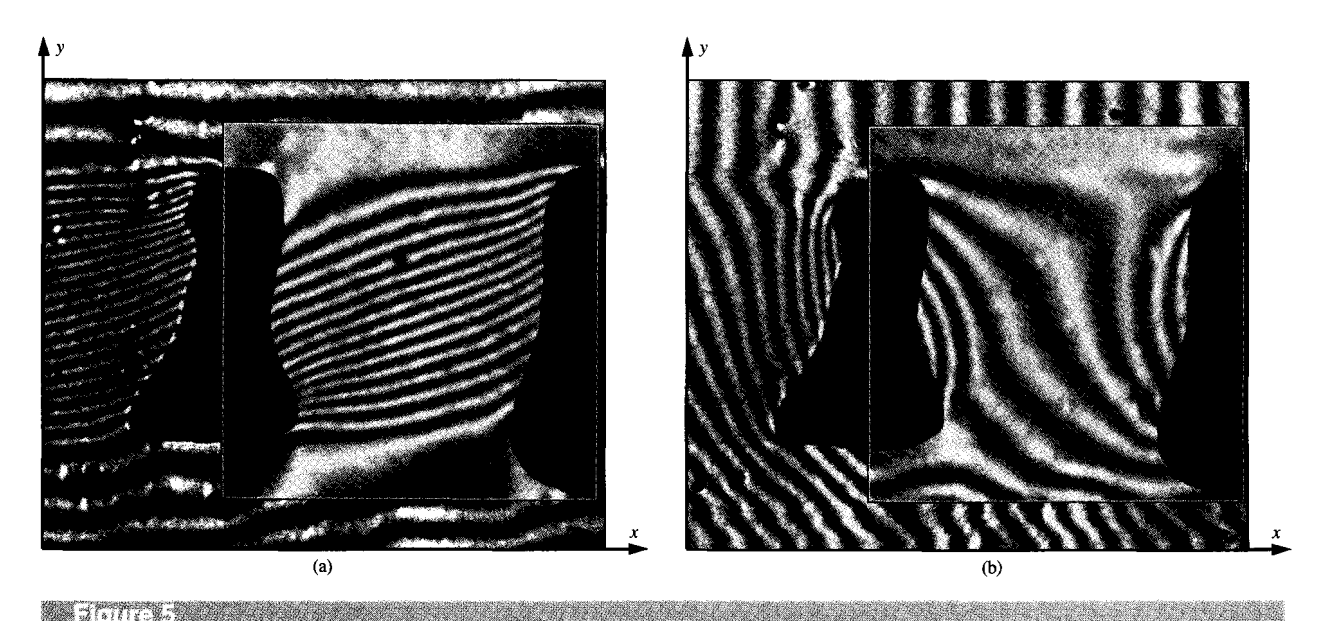
In the strain fields shown in Figure 6, noise at isolated points arose from grating defects, noises of the optical system, and edge diffractions from the material discontinuity. Most of these noises can easily be identified by comparison with the moiré fringes shown in Figure 3. Because wide diffraction windows were chosen to cover the entire spectrum of the moiré fringes, higher-order harmonics produced by the region of widely spaced moiré fringes (module area) are also included. In our case, the fourth-order harmonic is probably the highest order involved in the selected diffraction windows. This produces high-frequency noises in strain fields with an amplitude of $\pm 0.1\%$. These high-frequency noises may be eliminated by a low-pass filtering algorithm.

As discussed in Part I, the solder ball is deformed because of the relative motion between the ceramic module and the circuit board (global or macro effect), and because of the local thermal loading due to a mismatch of coefficients of thermal expansion across interfaces (local or micro effect). (Here "interface" refers to the interface between the solder ball and the board or the module.) The relative horizontal motion shears the solder ball (see Figure 10 in Part I), while the relative vertical motion compresses it (see Figure 9 in Part I). Uniform vertical motion produces only ϵ_{yy} , but horizontal motion produces two effects: pure shearing of the solder ball and bending of

654



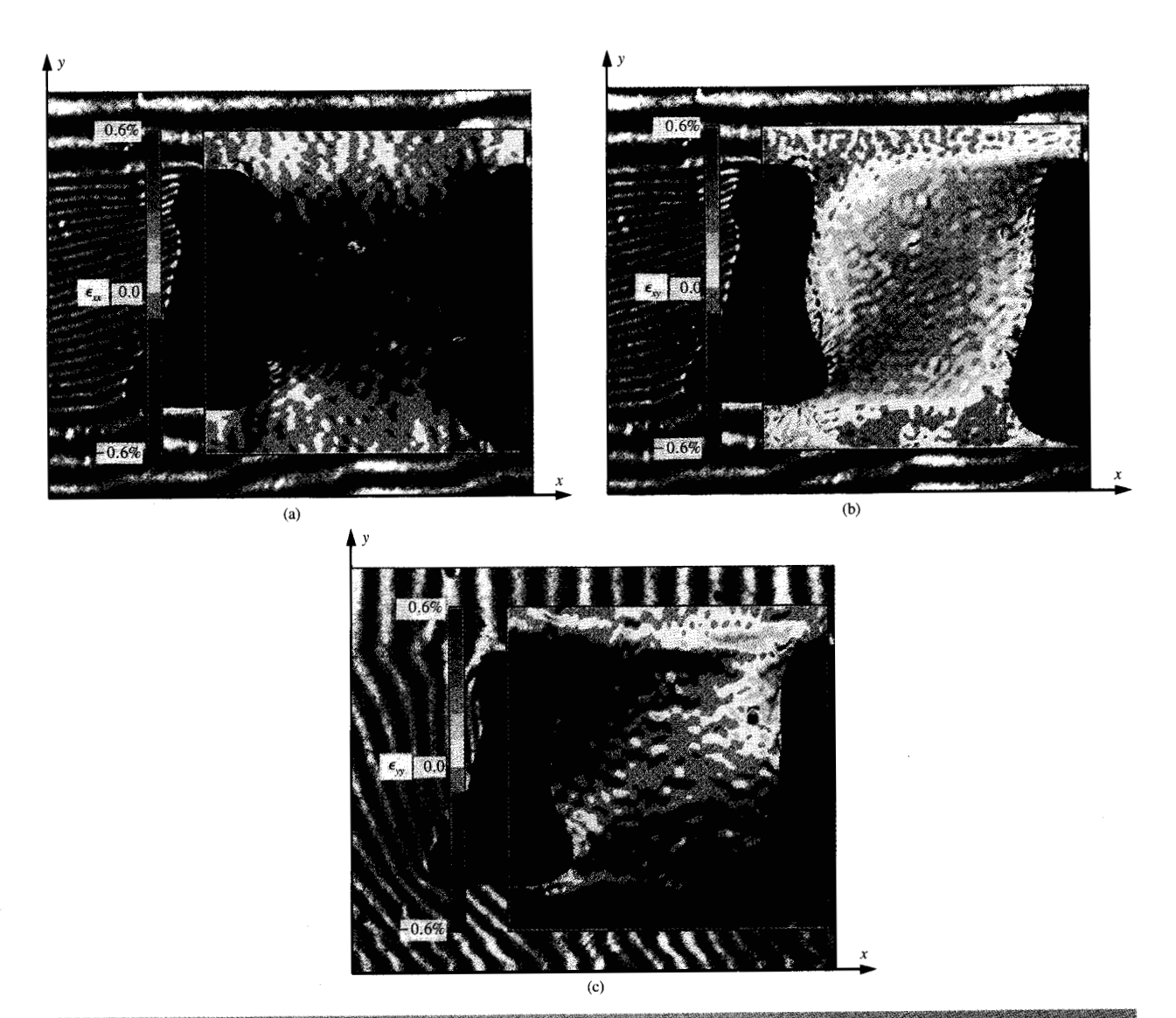
Calculated diffraction patterns for (a) horizontal displacement field; (b) vertical displacement field. The units along the axes are (pixel)⁻¹ and should be divided by LM (0.00218 m/pixel) to obtain actual frequencies.



Reconstructed moiré patterns after carrier patterns were removed: (a) Horizontal displacement field; (b) vertical displacement field.

the solder ball. The relative importance of the two effects depends mainly on the aspect ratio of the solder ball (i.e., height/diameter). In the extreme cases, pure shearing is totally dominant for a thin, wide interconnection, while

pure bending is dominant for a long column. For the SBC geometry considered here, the effects are almost equal. Therefore, a shear strain ϵ_{xy} within a solder ball is produced mainly by a pure shearing effect, and a normal



Elemira 6

Thermal strain fields in a solder ball: (a) ϵ_{xx} ; (b) ϵ_{xy} ; (c) ϵ_{yy}

strain ϵ_{yy} is produced mainly by a bending effect. To obtain the actual strains, the strains produced by the local effect should be superposed on the global strains. This matches very well the calculated strain fields shown in Figure 6. Because the local effect is limited to regions close to the interfaces, the shear strain ϵ_{xy} is almost constant in the center of the solder ball, with a value of around 0.3%. Maximum values of 0.5% appear at the top right and bottom left corners because of the superposition of local shearing across the interfaces, as discussed in Part I (see Figure 10 in Part I). The distribution of normal strain ϵ_{yy} in a solder ball is typical of strain produced by bending a short column with both ends fixed. Its maximum value (0.5%) appears at the top right corner.

Fatigue failure of SBC interconnections

The accelerated thermal cycling (ATC) test is a commonly used technique for evaluating the reliability of electronic packages. Figure 7 shows the typical shape of a failed solder ball located at the left side of an SBC package during an ATC test. This result was obtained by T. Caulfield at IBM East Fishkill. The temperature range was 0–100°C with a rate of 72 cycles per day. In this experiment, the average fatigue life among 80 specimens was approximately 1000 cycles. As shown in Figure 7, cracks appeared at all four corners of the solder ball, and propagated almost parallel to the interfaces. The primary failure occurred at the left side. The crack at the top left corner grew along a 10–20° direction from the horizontal

axis, while the others grew along a 20-30° direction from the horizontal axis.

To understand the failure mechanism involved in this experiment, one can study the principal components of the thermal strains given in Figure 6, as shown in Figure 8. The highest tensile principal strain appears at the top right corner. In this area, the principal normal strain ϵ_1 has a value of 0.6%, and the principal shear strain ϵ_{12} has a value of 0.6% with a principal angle of around -70° . Because this area is the highest-risk area, cracks initiate first in this area. Note that, because the solder ball shown in Figure 7 is located at the left of the module, strain fields for that solder ball are similar to those shown in Figure 8, except that they are reflected by a vertical axis. If the system is assumed to behave linearly with temperature, the maximum principal normal strain is 1.0%, and the maximum principal shear strain is 1.0% for a 100°C temperature change. As observed in the ATC experiment, the major failure occurred at the top left corner, and the crack propagated in a $10-20^{\circ}$ direction from the x_1 axis. This implies that the crack grew more during cooling cycles (the top left corner is under the highest tension) than during heating cycles (the top left corner is under compression), and that it propagated along an opening mode (mode 1) direction. Note that the direction of an opening mode is almost perpendicular to the principal direction.

Fatigue failure near the board side (bottom) was also observed. As shown in Figure 2 of [2], only one crack occurred near the board side in the solder ball during the ATC fatigue test. Calculating the plastic strain in the solder ball using a macro-micro model with the finite element technique, Corbin reported that the highest plastic strain in that area was 4.3% at 100°C, while it was 1.9% near the module side (Figure 13 of [2]). This differs from our experimental results, which show that the deformation near the board side is almost the same as that near the module side. This discrepancy may come from the strong dependency of solder properties on temperature, as shown in Figure 3 of [2]. Note that the temperature range in our experiment was from 82°C to 22°C. Because an ATC test is a fatigue test, a failure occurs not only near the module side but also near the board side in the solder ball, as shown in Figure 7, even though the deformation near the board side is smaller than that near the module side. However, the principal direction near the board side is around -40°, as shown in Figure 8(c). In this case, the cracking direction is closer to the maximum shear direction than to the opening direction. Therefore, a crack near the board side seems to be driven by a shearing mode (mode 2). This shear-dominant failure mode was also observed in a solder connection whose aspect ratio (height/diameter) was small, as in Figures 8 and 10 of [7].

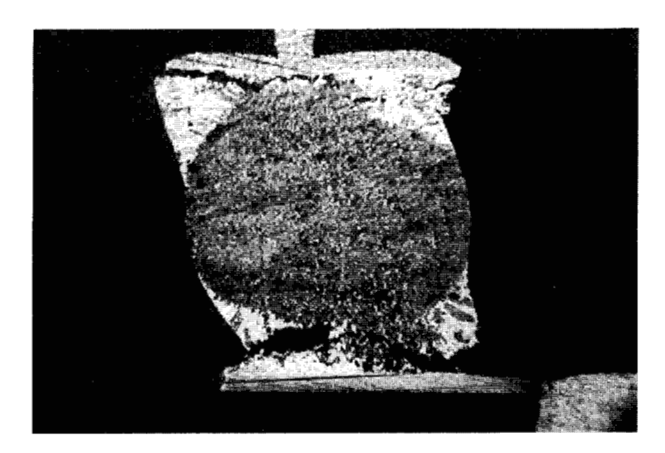


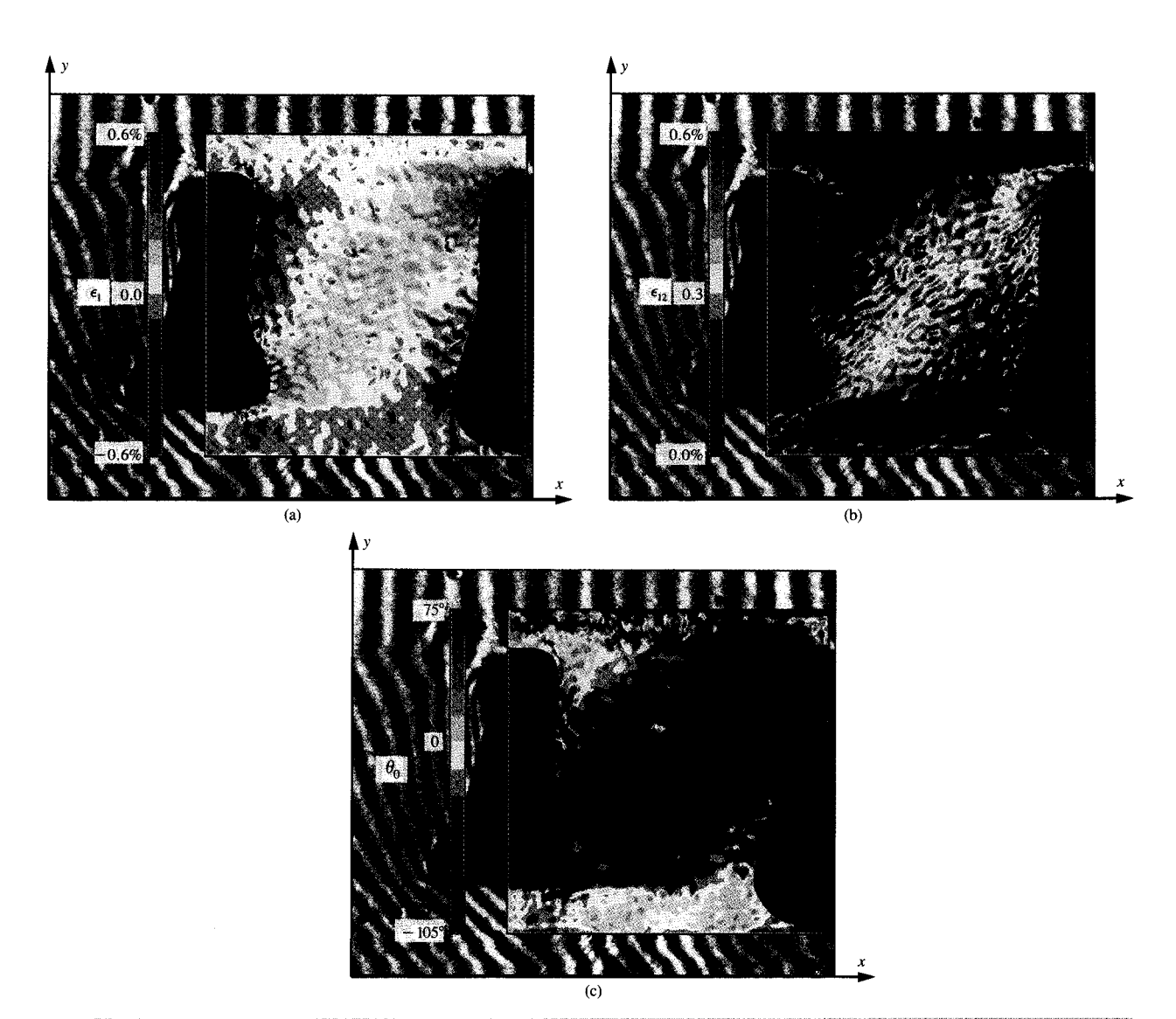
Figure 7.
Failed solder ball after ATC fatigue test.

Concluding remarks

A new image-processing technique, the computational Fourier transform moiré method, has been developed. This technique provides whole-field strains from digitized images of interferometric moiré fringes. Because an unwrapping process is not needed and the only process requiring human interaction is in establishing diffraction windows, the technique presented in this paper can easily be automated.

By use of software based on schemes described in this paper, whole-field strains of SBC interconnections between multilayer ceramic modules and printed circuit boards were obtained. The maximum normal strain ϵ_{yy} was 0.5%, and the maximum shear strain ϵ_{xy} was 0.5% for a temperature change of -60° C. Two risk areas where cracks may initiate were identified—one at the top right corner and the other at the bottom left corner. This was confirmed by an ATC fatigue test.

The components of the deformation of interconnections between a module and a board can be considered separately. One is the local effect due to the material mismatch across an interface (solder ball to module, and solder ball to board). The other is the global effect due to the material mismatch between the module and the board. Detailed discussions were presented in Part I [1]. Furthermore, the global effect can be partitioned into two major deformation modes; one is the pure shearing of a solder ball as a thin interlayer, and the other is the pure bending of a solder ball as a column. The strain distribution in the solder ball due to the global effect is the superposition of these two modes. The relative importance of the modes mainly depends on the aspect ratio (height/diameter) of the interconnection. The actual strain distribution is then the superposition of the strains



Hannes 8

Principal components of total strains in a solder ball: (a) Maximum normal component ϵ_1 ; (b) maximum shear component ϵ_{12} ; (c) principal direction θ_0 .

produced by the global and local effects. However, the local effect is limited to regions close to the interfaces.

For short interconnections, shear deformation is dominant and fatigue failure is driven by a shearing mode (mode 2), while for long interconnections, the bending mode is dominant and failure is driven by an opening mode (mode 1). For the solder ball considered in this paper, both modes are nearly equal. Therefore, both failure modes were observed. The dependency of fatigue life on the geometric shape of an interconnection, especially the aspect ratio, should be further investigated and will be reported in the future.

Acknowledgments

The authors thank Prof. K.-S. Kim at Brown University for his valuable discussions and T. Caulfield at IBM East Fishkill for providing experimental results.

Microsoft Windows is a registered trademark of Microsoft Corporation.

Videk is a trademark of Kodak Company.

ITI is a trademark of Imaging Technology Incorporated.

PS/Valuepoint is a trademark of International Business Machines Corporation.

658

References

- Y. Guo, C. K. Lim, W. T. Chen, and C. G. Woychik, "Solder Ball Connect (SBC) Assemblies Under Thermal Loading: I. Deformation Measurement via Moiré Interferometry, and Its Interpretation," IBM J. Res. Develop. 37, 635-647 (1993, this issue).
- J. S. Corbin, "Finite Element Analysis for Solder Ball Connect (SBC) Structural Design Optimization," IBM J. Res. Develop. 37, 585-596 (1993, this issue).
- T. W. Shield and K.-S. Kim, "Diffraction Theory of Optical Interference Moiré and a Device for Production of Variable Virtual Reference Gratings: A Moiré Microscope," Exper. Mech. 31, No. 2, 126-134 (1991).
- B. Han, "Interferometric Methods with Enhanced Sensitivity by Optical/Digital Fringe Multiplication," Appl. Opt. 32, No. 25, 4713-4718 (1993).
- Y. Morimoto, Y. Seguchi, and T. Higashi, "Application of Moiré Analysis of Strain Using Fourier Transform," Opt. Eng. 27, No. 8, 650-656 (1988).
- H.-C. Choi, A. F. Schwartzman, and K.-S. Kim, "Experimental Deformation Mechanics of Materials from Their Near-Atomic-Resolution Defect Images," *Mater. Res.* Soc. Proc. 239, 419-424 (1992).
- K. J. Puttlitz, "Preparation, Structure, and Fracture Modes of Pb-Sn and Pb-In Terminated Flip-Chips Attached to Gold Capped Microsockets," *IEEE Trans. Components*, *Hybrids, Manuf. Technol.* 13, No. 4, 647-655 (1990).

Received January 6, 1993; accepted for publication July 30, 1993

Hyung-Chul Choi IBM Microelectronics Division, 1701 North Street, Endicott, New York 13760 (CHOI at ENDVMTKL, choi@vnet.ibm.com). Dr. Choi received the Ph.D. in theoretical and applied mechanics from the University of Illinois at Urbana-Champaign. He joined IBM in October 1991 and has worked in the area of failure analysis for second-level packaging. In particular, he has developed an image-processing program for interferometric moiré fringes.

Yifan Guo IBM Microelectronics Division, 1701 North Street, Endicott, New York 13760 (YIFAN at ENDVMTKL, yifan@endvmtkl.vnet.ibm.com). Dr. Guo received his Ph.D degree in engineering mechanics from Virginia Polytechnic Institute and State University in 1989. After graduation, he was appointed as Assistant Professor in the Engineering Science and Mechanics Department at VPl&SU. He taught courses in mechanics and continued his research in the area of experimental mechanics and mechanics of composite materials. Dr. Guo joined IBM in 1990 as a Staff Engineer and began his research in the field of microelectronic packaging using laser interferometry and other experimental techniques. He recently received an IBM Division Award for his contributions in the development and applications of moiré interferometry in electronic packaging.

William R. LaFontaine, Jr. IBM Microelectronics Division, 1701 North Street, Endicott, New York 13760 (LAFONT at ENDVMTKL). Dr. LaFontaine received a B.S. degree from Cal Poly State University, San Luis Obispo, in 1985 and M.S. and Ph.D. degrees from Cornell University in 1988 and 1990, respectively, all in materials science and engineering. Since 1990 he has been at IBM, where he has worked as both Engineer and Manager in the area of micromechanics of plated structures. Currently, Dr. LaFontaine is a member of the Card Board Development Executive's staff.

Chun K. Lim IBM Microelectronics Division, 1701 North Street, Endicott, New York 13760 (LIMCKL at ENDVMTKL, limckl@endvmtkl.vnet.ibm.com). Dr. Lim is a Senior Technical Staff Member and Manager of Metallurgy and Micromechanics. He received the B.S. degree in mechanical engineering from the University of Missouri and the Ph.D. in engineering science and mechanics from Pennsylvania State University. He held a postdoctoral fellowship in materials science at the California Institute of Technology. Dr. Lim is a member of the Society of Experimental Mechanics, the American Society of Mechanical Engineers, and the Korean Scientists and Engineers Association in America. His current interests are materials and mechanics issues in microelectronics packaging. He has received an IBM Outstanding Innovation Award, an IBM Outstanding Contribution Award, an IBM President's Award, and the 4th Level Publications Achievement Award.